Master thesis

Tuning the electronic coupling of chiral graphene nanoribbons using the supporting surface

Master degree: Nanostructured materials for nanotechnology applications

Author: Alejandro Berdonces Layunta

Supervisors: David Serrate Donoso, Jorge Lobo Checa

2017 / 2018

Facultad de Ciencias
Universidad Zaragoza

icma
Instituto de Ciencia de Materiales de Aragón

Instituto Universitario de Investigación en Nanociencia de Aragón
Universidad Zaragoza

1. INTRODUCTION
    1. Motivation.
    2. On-surface synthesis.
    3. Graphene nanoribbons (straight and chiral).
    4. Edge states.
    5. Electronic decoupling by means of ultrathin insulating layers.
    6. Objectives
2. EXPERIMENTAL METHODS
    1. Sample preparation.
    2. Scanning Tunneling Microscopy.
    3. Scanning Tunneling Spectroscopy.
3. RESULTS AND DISCUSSION
    1. STRUCTURAL PROPERTIES
        1. cGNR/Au111.
        2. NaCl/Au111.
            1. NaCl deposition.
            2. Effect of temperature.
        3. Graphene nanoribbons and NaCl.
            1. Salt over ribbons.
            2. Annealing and lateral compression.
            3. Ribbons on ribbons.
    2. ELECTRONIC PROPERTIES WITH AND WITHOUT DECOUPLING
        1. Edge states on cGNR/Au111.
        2. Comparison when decoupling ribbons.
            1. Spatial resolution.
            2. Energy resolution of edge state and valence band onset.
4. CONCLUSIONS
5. REFERENCES
6. ANNEXES
    1. Acronym index.

1. INTRODUCTION

1.1. Motivation

Graphene is a material of great versatility[1,2]. For instance, the sp_2 covalent bonds linking the C atoms in extensive 2D sheets confers great mechanical strength[3]. Moreover, it exhibits huge electronic mobility and sensitivity of conductivity to external parameters, which makes it interesting towards microelectronics[4], as well as in the energy sector[5,6,7] and data storage. All these properties add to the prospect of numerous applications in the field of materials science.

Notably, the electronic properties of graphene are tunable[8]. When graphene shrinks in one of its dimensions to form ribbons, its conductivity decreases and transforms from metallic to semiconductor below a critical width[9], while still preserving the appealing properties of its extended form. Thus, it is of interest to the field of molecular electronics in order to build nanotransistors.

The conductivity dependence of graphene nanoribbons on the width has a characteristic length scale in the range of Angstroms[8]. Therefore, an extremely precise manufacturing method is required. On Surface synthesis is a bottom-up approach that allows graphene manufacturing with atomic precision featuring exact width and edge geometry[10]. This is nowadays far better than the top-down methods, whose size limit is currently on the scale of tens of nanometers[11] and are prone to produce spurious effects due to sample damage.

Nanotechnology with such precision requires cutting-edge experimental infrastructures. Based on state of the art Scanning Tunnelling Microscope (STM) of the Laboratorio de Microscopías Avanzadas (LMA), the electronic structure of the different parts of the nanoribbons has been locally studied, facilitating a deeper comprehension of the quantum nature responsible for their superior properties.

1.2. On-surface synthesis

This type of chemical reactions are classified in chemistry as dry-synthesis because no solvent is used for the processes[8,12–14]. Contrarily to wet chemistry, reactives are deposited onto a solid surface under vacuum conditions before reacting. The substrate acts as a heterogeneous catalyser, interacting with the molecules and reducing the energetic barrier required for the reactions. The lack of solvent allows molecules to adapt their

conformation and migrate over the surface following the two dimensional character of the substrate. Depending on the precursor design, they can be forced to react just in one position, reducing the number of subproducts and achieving an almost ideal yield[8,12–14]. As will be shown, the bottom-up strategy allows to obtain well-defined, atomically precise covalent molecular structures[13,15–17].

Ultra high vacuum (UHV) conditions for on surface synthesis generates highly controlled environments and increases the activity of catalysers. UHV reduces the uncertainty caused by the effect of uncontrolled factors such as humidity, residual gas composition or unstable temperature. Besides using different substrates can lead to different products or stabilize reaction intermediates, providing ways to improve the synthesis methods.[18]

On-surface products are generally strongly bound to the surface due to the extensive substrate-molecule interactions. This allows us to study their nature, assemblies and even the intramolecular structure with scanning probe techniques[13,15].

1.3. Graphene nanoribbons

An important family of on-surface synthesized structures are graphene nanoribbons (GNRs). These are one-dimensional (1D) chains generated from carbon-based monomers[8,13,14,19–21]. Carbon stabilizes its electronic configuration through covalent bonds when forming four bonds with nearby atoms. To stabilize them depending on the kind of bonds, there are three possible hybridizations: sp_1, sp_2 or sp_3. GNRs are achieved by sp_2 orbitals, which exhibit a trigonal plane conformation with 120° angle between bonds. If six of these carbons bound in a hexagonal shape, they form a benzene-like ring with sp_2 orbitals. When these units extent periodically on two dimensions, quasi-free *p* orbitals remain perpendicular to the C bonds and generate the two-dimensional (2D) delocalized electronic states across the surface, the so-called π-states. An infinite 2D set of these hexagonal rings gives rise to graphene, which exhibits very different properties compared to graphite. The π-states of each carbon ring combine into bands that result in a Dirac type 2D conductor[22].

When narrowing the graphene in one dimension, the Dirac-like band splits into conduction and valence bands, opening a gap between them. The formed ribbon becomes semiconductor, exhibiting a band gap dependence with its width: the narrower the ribbon, the larger the gap[8]. The lateral size of GNRs (30º rotated) can be controlled in bottom-up synthesis by choosing the right precursors. Choosing the position of chemical radicals in

these precursors allows GNRs to polymerize just in one direction (along the so-called long axis or growth direction)[13,20,23].

Another characteristic that defines GNRs is the shape of their edges (see Fig. 1.1). If it is parallel to the graphene lattice directions, their edges show a zigzag pattern (Figure 1.1, left). The other high symmetry GNRs (30º rotated) are referred to as armchair. For this shape, the edges exhibit "lobes" caused by the alternating rings (see Fig. 1.1, right).

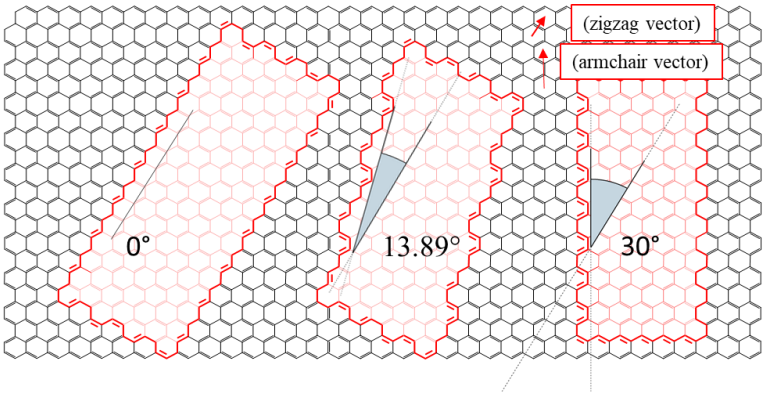

Figure 1.1. *Schematic graphene nanoribbons with different edge termination indicated by the relative angle between a main hexagonal axis and the edge termination: zigzag (0º) (left), chiral with 1 armchair/3 zigzag (13.89º) (middle), and armchair (30º) (right).*

A combination of zigzag and armchair edges leads to an infinite variety of ribbons with mixed types of edges. Their nomenclature (*n*,*m*)-GNR, regardless of ribbon size, counts each ring type in the periodic unit, first zig-zag (*n*,*0*) and then armchair (*m*,*m*) graphene lattice vectors. These vectors are necessary to define a direction parallel to the ribbon longitudinal growth axis[25]. The precursors used in this work are (3,1)-GNR, which means 2 zigzag rings for each armchair. The growth direction is 13.89° away from one graphene high symmetry axis. This characteristic will make them chiral graphene nanoribbons (cGNR) on a surface[26] (see Fig 1.2).

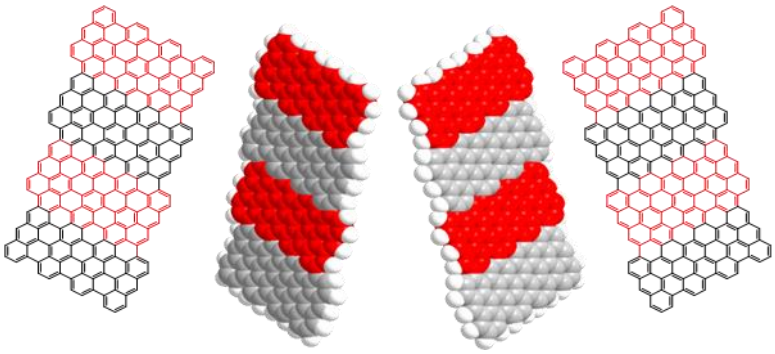

Figure 1.2. *Adsorption-induced chirality: The same molecule (represented by the 3d models) with planar symmetry, led to a couple of enantiomers depending on the face adsorbed. On a surface, just perpendicular symmetry elements are allowed.*

1.4. Edge states

Extensive materials present different properties and electronic structures at their borders. For three dimensional materials, like gold, the largest terminal regions correspond to the surface, and are characterized by exhibiting two dimensional surface states[27]. For prototypical 2D materials, such as graphene, special electronic states are found at their 1D borders[28,29,30]. Moving to GNRs, when they are zigzag terminated, the valence (VB) and conduction bands (CB) get closer before collapsing at the vacuum[25,28]. At the Dirac point, the top of VB and the bottom of CB meet causing the density of states to increase abruptly at one specific energy that lies close to the Fermi level. This singularity in the LDOS are known as ***edge states*** because their intensity concentrates at the graphene zig-zag terminations[9,25,30].

In tight binding theoretical calculations, the edge states are described for a graphene patch as follows: *n* C atoms with *n/2* valence orbitals and *n/2* conduction orbitals that combine to form *2n* hybrid states (counting different spins on the same orbital as different states) of the same energy half occupied by *n* electrons (Fig 1.3(a)). Due to the Coulomb repulsion, these degenerated *2n* states split in spin polarized occupied and unoccupied states[29] (Fig 1.3(b)). In the new hybrid orbitals, these split electronic states exist independently at both sides of the ribbon. Nevertheless, when the ribbon is narrow enough, states at both sides of the ribbon couple to each other resulting in a magnetic ordering of spin up and down states located at different sides of the ribbon[29] (Fig 1.3(c)).

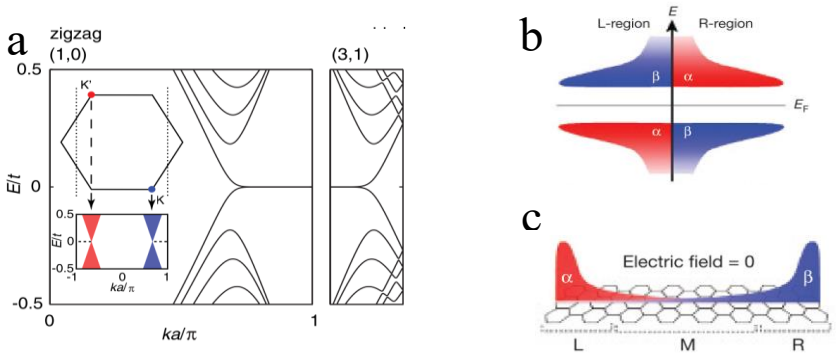

Figure 1.3. *a) Tight binding band structure without e-e interaction. Edge states appear around the Fermi level by convergence of valence and conduction states on pure zigzag ribbons and (3,1)-cGNR[28]. b) On each side, the coulombic repulsion causes an energy splitting by spins. For narrow enough ribbons, both sides are coupled antiferromagnetically with opposite spins[29]. c) Spatial distribution of edge state spin polarization on a zigzag ribbon[29].*

In short, stable electron pairs (spin up and down) couple in opposite sides in order to avoid coulombic repulsion[25,28]. When both sides are close enough, there is an antiferromagnetic alignment between them, giving rise to a net, finite ferromagnetic moment at each edge.

The presence of an edge state is interesting for various reasons. They are 1D electronic states composed by Dirac quasi particles, with large electronic mobility and they are spin polarized, sparking the interest within the field of spintronics. These states are found around the zero potential, so they could make the ribbon edges have metallic conduction if the Fermi level crosses them (see Fig. 1.3). Taking into account that edge states are present just on zigzag terminations[25], the balance between metallic conduction of the edge and semiconductor behaviour of the ribbon can be tuned by adjusting the degree of chirality of the atomically precise edges[25] when they are generated by bottom-up techniques.

1.5. Electronic decoupling by means of ultrathin insulating layers.

The intercalation of a thin insulating layer between the molecular structures and the metal is quite useful to study the resulting electronic properties after synthesis, as the direct contact with the metallic substrate is known to modify them[17,31]. The electronically decoupled molecules will show similar properties to the ones in free standing conditions[17]. However, the chemical reactions of the precursor generally fails on the insulator surface because the metallic substrate takes active part as catalyser. There have been reaction strategies based on anchoring groups of monomers on the insulator film or on the catalytic role of defects inside insulating materials to trigger the reactions.

In the last years a different approach has been undertaken to decouple GNRs. It has been shown that the STM tip can be used to carry the molecular structures (GNRs) from the metallic surface where the reaction took place, to an insulating layer of NaCl.[14,17,19,22,32] In this master's thesis, we show that it is possible to substitute the NaCl by **another identical nanoribbon**. Since they are very narrow (see section 1.3), they will exhibit the necessary semiconducting behaviour as to decouple the top ribbon from the Au(111) substrate[9]. Different driving mechanisms are in this work is contemplated: Instead of manipulation forces between STM tip and GNRs, our approach is thermodynamically driven, since the dragging is promoted by the thermal agitation of NaCl coexisting in the surface.

1.6. Objectives

The aim of this work seeks the experimental accomplishment of these points:

- Synthesize chiral (3,1)-GNR from the selected precursor on Au(111).
- Study their morphology and electronic structure, focusing on the identification of expected edge states.
- To develop new methods to decouple the GNRs from the substrate by addition of NaCl and determine its effectiveness. Decoupling the molecular structures would be used both to study the ribbons with higher resolution, and to release them from the substrate.

2. EXPERIMENTAL METHODS

2.1. Sample preparation

GNRs are synthesized using the catalytic properties of a clean surface of a Au(111) single-crystal. First, the cleaning of the gold surface is made by removing the top superficial layers of metallic atoms with a 5 keV ion beam of argon during 10 minutes followed by subsequent annealing (10 minutes) at 550 °C using an e-beam heater operated at 800 V and 5-8 mA emission current that heals and flattens the surface. Two types of Argon sputtering guns (a diffuse beam sputter gun and a focused sputter gun) have been used. A final cleaning cycle is performed with 1-2 keV to minimize the ion damage and obtain an optimal surface.[8,10,16,25–27].

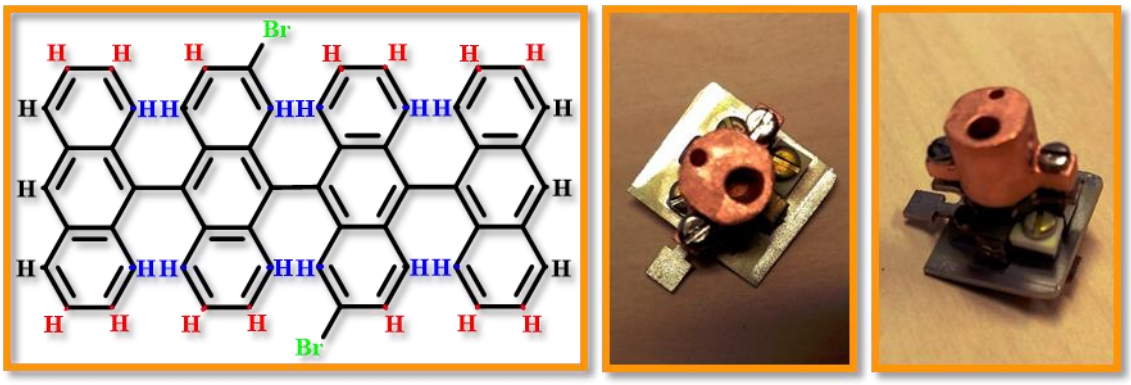

***Figure 2.1**. The precursor molecule is dBQA (left) is placed into the crucible of the evaporator (right). After regenerating the chamber pressure, molecules are heated up by a resistor wrapping a ceramic element inside the Cu crucible visible in the photograph till they sublime at an optimal rate.*

After atomically cleaning the substrate, precursor molecules placed into the ultra-high vacuum are evaporated by resistive thermal sublimation at about 300 ºC, measured with a calibrated thermocouple on the evaporator set-up. The precursors used in this work are 2",3'-dibromine-9,9':10',9":10",9"'-quateranthracene (referred to as dBQA, see Fig. 2.1, left) and were synthesized by the group of Prof. Diego Peña (Universidad de Santiago de Compostela). After deposition onto Au(111), the precursors are free to diffuse over the surface and form different macrostructures. Controlling parameters of the evaporation are the voltage and the current applied to the resistor (Fig. 2.1, right), whereas the measured variables are the thermocouple temperature on the stage of the crucible (not representative, but reproducible) and the evaporation rate measured with a quartz microbalance facing the outlet of the evaporator. A quartz microbalance is a piezoelectric resonator whose frequency shift depends on the adsorbed mass onto the quartz. The evaporation rate was roughly 0.5 graphene monolayers per minute (ML/min). Details about the polymer formation will be provided in section 3.1. In the case of NaCl evaporation, crucible temperature was about 570 ºC (I=1.8 A) and resulted in a deposition rate of around 12 NaCl ML/min.

After deposition of the precursors and/or NaCl, we performed post-annealings in UHV by mild e-beam heating (500 V, 1 to 1.8 mA) to thermally promote atom and molecule mobility that lead to sample modifications, i.e., chemical reactions for the precursors and mass transport and agglomeration for NaCl. Sample temperature during thermal treatments was measured by a pyrometer outside the UHV chamber focused at the Au surface.

2.2. Scanning Tunnelling Microscopy (STM)

Scanning Tunnelling microscopy is the main technique used for data acquisition in this work. It consists of a metallic tip controlled by piezoelectric actuators of two types: one tubular piezo for the *x/y/z* fine scanning and image acquisition, and a set of walkers (small electrical motors) for coarse positioning. The tip can be made of different metals depending on the requirements. In our case we used a metal tungsten tip, which was sharpened to the nanoscale by electrochemical etching[33] (NaOH solution 2M with a steel counter electrode). At the end of the process, the last atoms of the apex, which are

responsible for the STM resolution, are in-situ modified by controlled indentation into the metallic substrate.

Once the tip is placed in close proximity to the substrate, due to the quantum tunnelling effect, the applied potential (referred to as Vbias) between sample and tip exchanges electrons from the occupied band of one of the leads (tip or sample) to the unoccupied states of the other[34–39]. The density of electrons transmitted is measured as a tunnelling current ranging from a few picoAmperes to tens of nanoAmperes thanks to the I-V amplifier[19,39–41] (see Fig. 2.2). When measuring in constant current mode, the current is the input of the feedback controller, whereas the *z*-height is the feedback output that maintains the current constant, which is recorded to build a 3D rendering of the topography. When the feedback is deactivated, measuring in constant height (C.H.) mode, the tunnelling current (I_t) is the recorded magnitude that forms the image[15,42].

For the very simplified case of small Vbias (compared to the tip and sample workfunctions), very low temperatures (near 4 Kelvin), and tip and sample electronic structure described by plane waves, the relation between the tip-sample distance (Δz) and the tunnelling current (I_T) follows this well-known expression[43]: $I_T \propto e^{-2k\Delta z}$. Due to the exponential attenuation of the tunnel effect with distance, STM can yield picometer resolution in the *z*-axis and subatomic resolutions on the *x,y* axes, allowing us to study and identify intramolecular structure of the synthesized polymeric products.

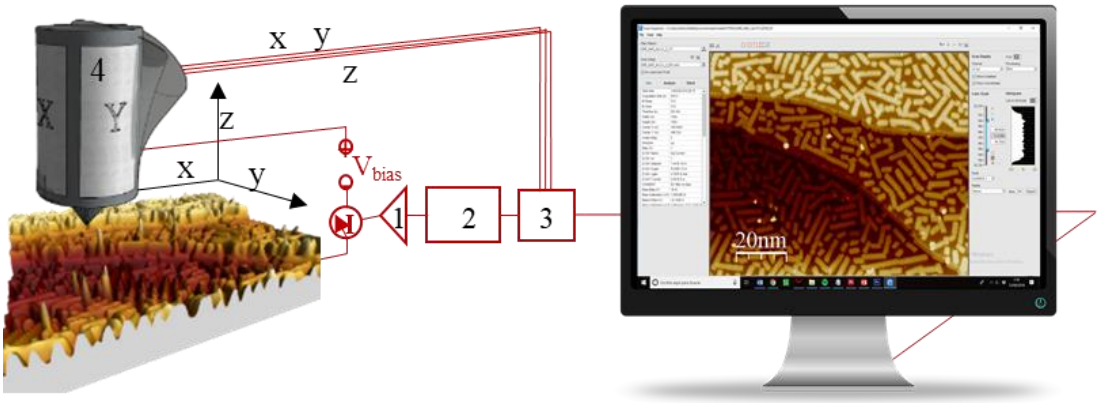

Figure 2.2. *STM scheme with its different electronic components.* ***1,2-Current to voltage amplifier****. Transforms the minute flowing current into a measurable proportional voltage.* ***3-Control unit.*** *Adjusts the piezos movement to the parameters & current feedback.* ***4-Piezoelectric tube.*** *Changes its form with the voltage applied to scan the surface with subatomic precission.*

2.3. Scanning Tunnelling Spectroscopy (STS)

Scanning Tunnelling Spectroscopy is a modification of the STM technique. Using an oscillator, a periodic AC modulation of Vbias is introduced to measure the variation of the current with the voltage (dI/dV), i.e., the tunnelling differential conductance. This conductance is proportional to the local density of states (LDOS) when measured at a particular sample position for a range of Vbias[8,14,30] (see Fig. 2.3(a)). The conductance also depends on the tip-sample distance (defined by the feedback setpoint where it was open) and on the oscillator parameters (such as amplitude of the AC signal). Thus, the dI/dV obtained at a specific energy/position is proportional to the LDOS with a proportionality factor dependent on a number of technical parameters. For this reason, the vertical axis of dI/dV spectra is generally represented in arbitrary units (A.U.)[12].

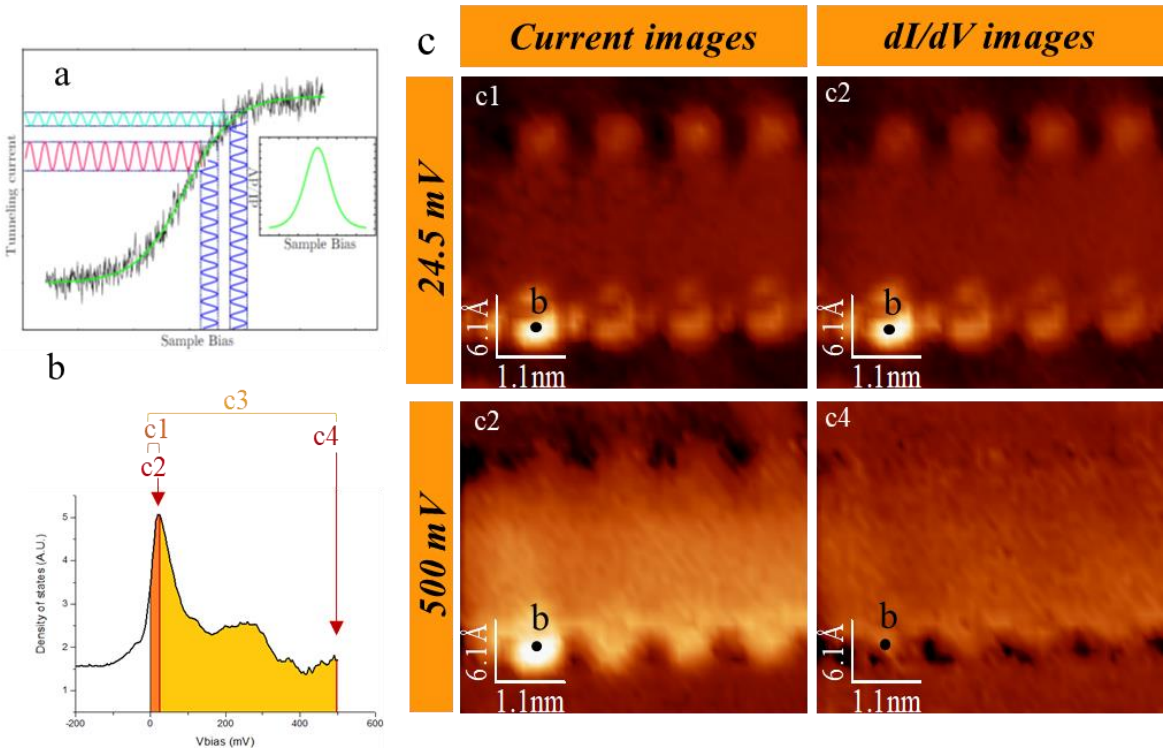

Figure 2.3. a) *Scheme of LDOS determination. Modulation of the voltage (dV, blue) produces a current oscillation (dI, red and light blue) directly related with the density of electronic states and current vs Vbias slope*[44]*.* ***b)*** *LDOS spectrum of point b.* ***c)*** *Comparing dI/dV maps (LDOS at a specific energy) vs current maps (integrated LDOS shown by the coloured areas enclosed by the spectrum). (c1 and c2) Different images of a state around 25 mV on the b spot. When taken around the peak near the Fermi level both images are quite similar. When acquired at 500 mV, current images (c3) show electronic states from 0 mV to 500 mV, so the peak is visible as a bright area (c3). Nevertheless, the dI/dV image just shows states at 500mV (c4), so the b area is not bright anymore. dI/dV maps are useful for imaging states at specific energies. Setpoint: -1V, 200pA.*

If an area is slowly scanned at constant voltage and height with the oscillator enabled, the dI/dV image obtained is proportional the sample LDOS at that specific energy with respect to the Fermi level. It is an improvement compared to recording only I_t in constant height scans, because (as shown in Fig. 2.3) this latter signal contains the integral of all electronic states from the designed Vbias to the Fermi level[10,17,31,45].

3. RESULTS AND DISCUSSION

3.1. STRUCTURAL PROPERTIES

3.1.1. cGNR/Au111

The cGNRs are formed using the dBQA precursor (Fig 3.1). When deposited on Au(111), this monomer is not planar on the surface, but has an alternated configuration of its inter-antracenic sub-units due to the steric hindrance between overlapping hydrogens (see Fig. 3.1(a,b)). The most probable conformation maximizes the interaction between bromines and the Au(111) (Fig 3.1(a)).

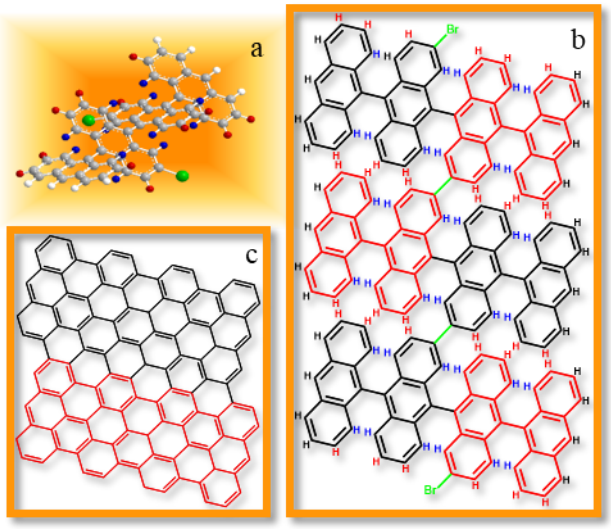

Figure 3.1. a) *monomer non-planar conformation forced by hindrance. Green Br atoms will be removed after polymerization.* ***b)*** *Top view of pre-planarized polymer made up of three units* ***c)*** *Fully planarized two-units ribbon where the blue/red H atoms in (b) have been cleaved and new C-C bonds formed.*

The reaction runs in two steps: The first is the well-known Ullmann coupling where the substrate catalyses a double-debromination of the precursors and generates radicals[10,12,16,46]. These radicals are not bound to the gold, but are able to wander over the surface to bind to other radicals (green bonds in Fig. 3.1(b)) giving rise to polymerised chains.[13] The second step is the cyclodehydrogenation (CDH) that provides the final form to the nanoribbons. Here, trans-monomeric hydrogens and inter-monomeric hydrogens (respectively represented in blue and red in Fig. 3.1(b)) are removed from their carbons, whose free bonds can now bind to each other and conform a fully planar specimen. Whether both reactions (intra and inter) are simultaneous or happen on two steps still

needs to be clarified. The final ribbon shown in Fig. 3.1(c) stays parallel to the surface to maximize the interaction of the π-orbitals of the phenyl rings with the substrate. Terminal bromine vacants at the two opposite sides where the ribbon growth stops cannot remain as radicals, so they must be saturated by reacted hydrogens from CDH or by surface Au atoms.

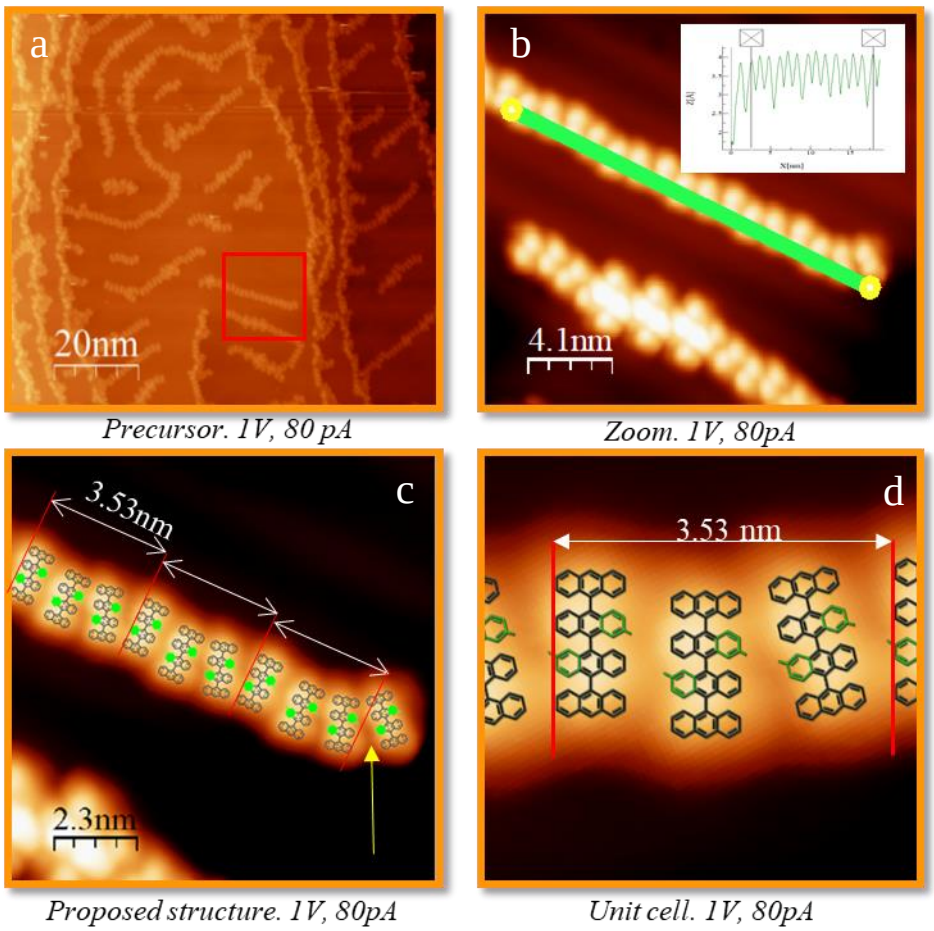

Figure 3.2. *Arrangement of the molecular precursors before reacting (no debromination).* ***a)*** *Large survey showing that the molecule lines follow the herringbone valleys.* ***b)*** *Molecular trios ordered periodically. Lattice size: 3.53 nm. According to the inset the maximum apparent height is 0.4 nm.* ***c)*** *Unit cell determination. Green rings mark bromine-bonded rings. Yellow arrow indicates a twist on the gold herringbone. d) Zoom of one unit cell.*

Before polymerization (Fig 3.2), just after the precursor evaporation, molecules arrange themselves following the channels of the Au(111) herringbone reconstruction[27,40],which are natural channels that appear on Au(111). The absence of Br on the surface discards spontaneous de-bromination right after precursor deposition when the substrate is kept at room temperature. The unit cell is formed by three molecules with the first two being parallel to the herringbone lines (Fig 3.2(b, d)) so that their rings follow the principal

direction of gold atoms, which provides a better interaction with the substrate. The monomers are shifted by the length of approximately a carbon ring to avoid hindrance between neighbouring bromines. To remain within the herringbone channel, the third molecule lies in between their two positions. To increase bromine separation, it occupies a larger longitudinal space and twists itself roughly 14° from the other two aligned monomers.

In order to generate the ribbons from this precursor, a thermal treatment is required. We find that annealing up to 317ºC results in non-fully planar chain formation (see Fig. 3.3(b)). The presence of bromine as bright dots (yellow arrows) next to the chains confirms de-bromination. At this temperature, the CDH that leads to the chain planarization is starting, but is still incomplete. Reaching 322ºC results in atomically defined and planar cGNRs (Fig. 3.3(c)), suggesting a small temperature window around 320ºC for this planarization process to take place.

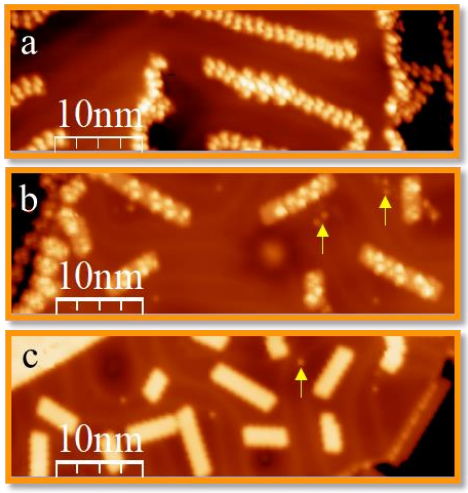

Figure 3.3. *Planarization of polymeric chains through cyclodehydrogenation. 1V, 50pA:* ***a)*** *Before heating;* ***b)*** *After heating up to 317°C with pyrometer;* ***c)*** *Maintaining the sample at 322°C during 3 min. Yellow arrows: side bromines products from the Ullman reaction.*

Ribbon dimensions have been obtained from measurements of 50 ribbons. The apparent height at Vbias from ±1V is 0.20 ± 0.01 nm, showing a noticeable reduction with respect to the non-planar precursor. As shown in Fig. 3.4(b, c), the average period at the edge is $p = 6.245b = 0.890 \pm 0.005$ *nm*, so we obtain a carbon bond length of $b = 0.143 \pm 0.001$ *nm*, which is in perfect agreement with the values from literature for graphene C-C distance[47]. Therefore, the resulting ribbon matches the expected structural model derived from the precursor reactivity (Fig. 3.4(c)). The corresponding theoretical width yields $w = 10.82b = 1.55 \pm 0.01$ *nm*, which does not coincide with the experimental average width at half height of 2.23±0.1 nm. This difference suggests that diffuse edge orbitals spill out

of the borders, as is usual in accurate STM measurements of atomically sharp terminations.

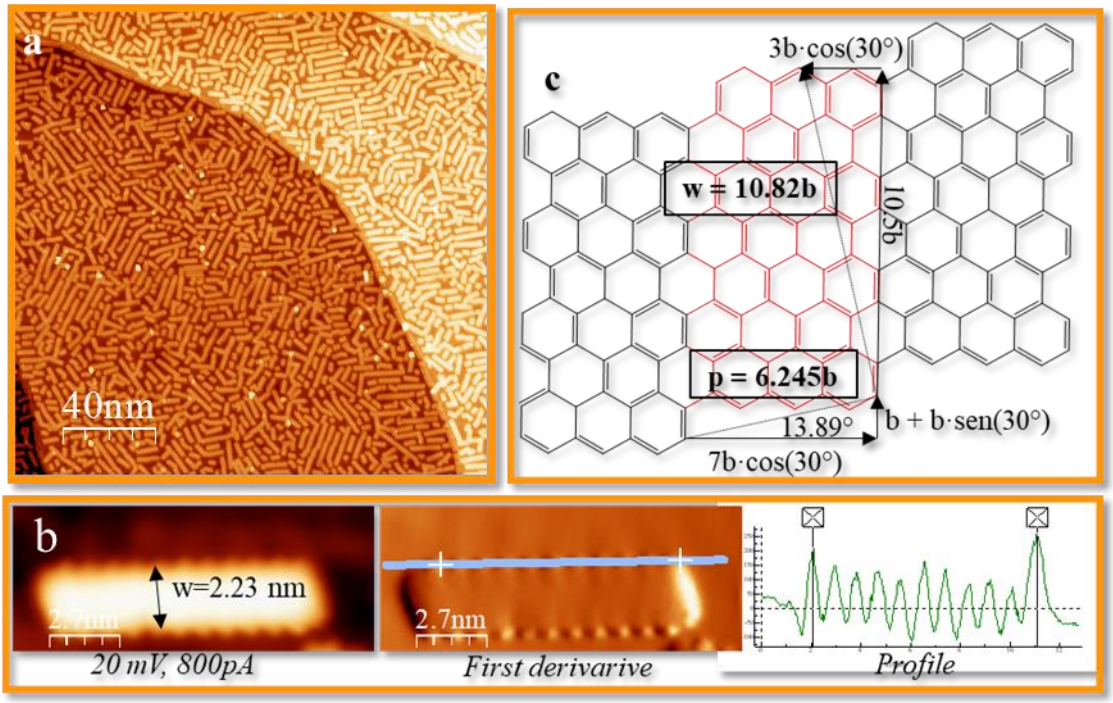

***Figure 3.4**. **a)** Large survey of a sample covered by c-GNRs. **b)** Example of the measure of a ribbon period with the first derivative (dz/dx) of a topography image and the corresponding line profile at the edge. **c)** Calculation of a ribbons' period (p) and width (w), referenced to the perpendicular direction of growth in terms of the carbon bonds (b).*

The structure was confirmed by images taken with a functionalized tip[33,48] (Figure 3.5). These images are acquired with a Cl ion from a nearby NaCl island (not shown in the

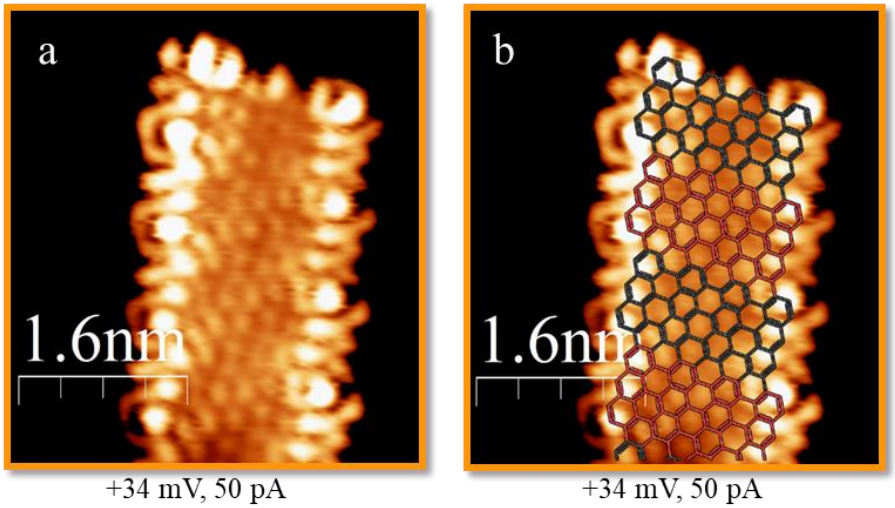

***Figure 3.5. a)** Image of a ribbon with a Cl-funcionalized tip. **b)** Superposition of the GNR model that agrees with the atomic structure.*

zoomed image), sticking at the edge of the tip that allowed us to observe the hexagonal lattice of the ribbon.[33]

The influence of the substrate is strong when probing cGNRs with a metallic non-functionalized tip. Delocalized orbitals extend over the whole polymer, hindering the visualization of the internal structure of the chain. Maximizing the tunnel current resolution by reducing the Vbias and approaching the tip allows observing the internal cGNR structure (see Fig. 3.6). However, if the tip is approached too much, it is likely to move or rip the ribbon from the substrate.

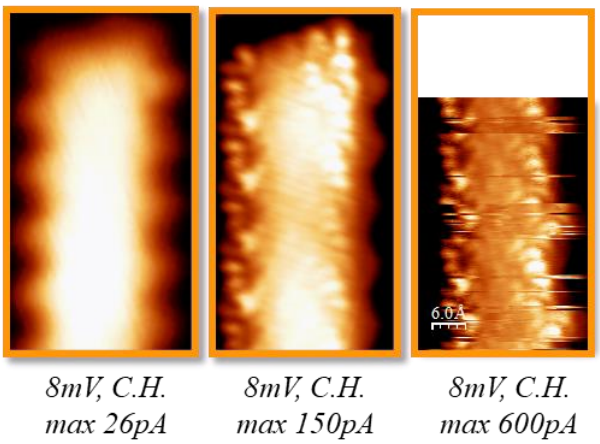

Figure 3.6. *Three constant current tunnelling images of the same ribbon acquired at different constant heights. As the tip is approached to the surface, the internal structure starts to become defined. However, if the tip gets too close, tip-sample forces are able to shake it over the surface, as observed by the noisy horizontal lines in the right panel.*

The proximity of the ribbon wave functions and the Au surface state gives rise to hybridized states with enhanced metallic character. This proximity effect precludes the observation of the semiconducting properties and edge states predicted for these nanostructures[9], at least when using regular metallic tips. For this reason, other strategies must be applied to study the intrinsic electronic structures of the ribbons. In particular, we tried to decouple them from the substrate by using NaCl.

3.1.2. NaCl / Au(111)

3.1.2.1. NaCl deposition

Layers of NaCl are deposited on the surface of Au(111) to electronically decouple the nanoribbons from the metallic surface. However, before describing these results, we report the NaCl growth onto Au(111), whose sublimation was described in section 2.1.

NaCl tends to grow forming first a bilayer and extending over the surface like a carpet across the defects and step edges. The herringbone reconstruction of gold can still be

visible through salt layers[49] (Fig. 3.7 (a)). For this reason, visualizing the herringbone is not an indicative of having a bare gold surface underneath the tip.

When NaCl is evaporated over a substrate at room temperature, it grows on a square lattice stacking with the (001) plane parallel to the surface, and forming 2, 3 or even 4 ionic layers (Fig. 3.7). The monolayer is never observed. The height reduction after addition of each layer from the first two layers (see table in Fig. 3.6d) is related with its insulating nature. This apparent height at Vbias= -2.5 V is not even close to the real one of a free standing bilayer (2.82 Å)[49]. This is due to the STM sensitivity to the electronic structure of the overall tunnel gap, since for intermediate insulating structures, the tip has to get much closer to the surface to reach the same tunnelling current than for metals.

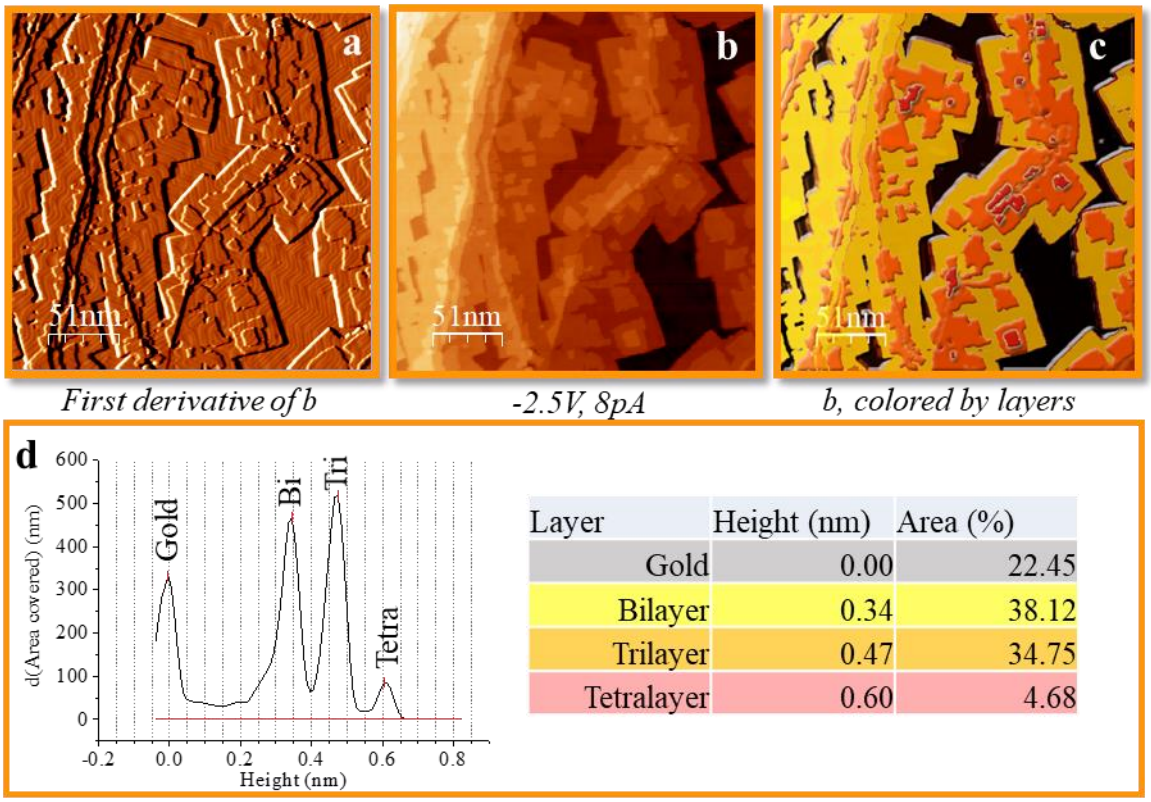

Figure 3.7*. Analysis of NaCl deposited at room temperature onto Au(111) (12 seconds, 570 ºC).* ***a)*** *First derivative (dz/dx) exhibiting the herringbone reconstruction through the NaCl.* ***b)*** *original image and* ***c)*** *false coloured image showing the different NaCl layers: Bilayer (yellow), trilayer (orange) and fourth-layer (red) over the gold substrate (dark).* ***d)*** *Coverage analysis is summarized in the table. Surface coverage of each layer: the area under each peak represents the surface area covered by each z value of the image.*

The NaCl(001) growth was confirmed studying its unit cell from images showing atomic resolution. Measurements of the corresponding Fourier transform were performed in reciprocal space, showing a clear difference in the lattice symmetry between both surface terminations. Au(111) features an atomic hexagonal lattice (Fig. 3.8, left) and it is used to calibrate *x,y* piezoelectric transduction coefficients of the scanner, whereas bilayer and trilayers of NaCl exhibits a square lattice yielding a chlorine-chlorine distance of 4 Å (identical to reference[50]). Note that at Vbias far from fermi level only Cl ions are visible in STM images of NaCl[33,48,49,51–54].

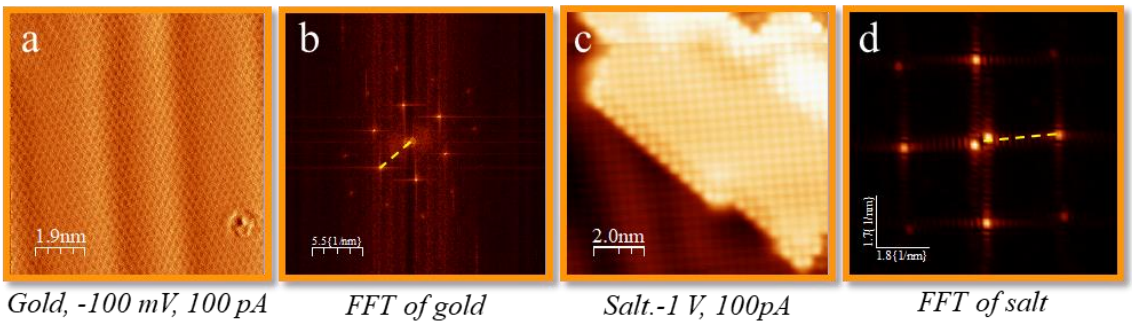

Figure 3.8. *Unit cell sizes and atomic distances of the Au(111) (a) and NaCl (c). The average periodic distances were calculated through the Fast Fourier Transform (FFT) of the images with atomic resolution. b) FFT of (a), extracted surface lattice parameter of Au (111)=2.88 Å. d) FFT of (c), lattice parameter of NaCl(001)=4.0 Å.*

3.1.2.2. Effect of temperature

We have found that NaCl tends to agglomerate in larger patches when increasing the temperature of the supporting substrate, T_{NaCl}. When 1.8 ML are deposited over the cold Au(111) substrate (Fig 3.9, left), islands forming small patches with irregular edges cover the surface. On the other hand, when NaCl is deposited at room temperature (fig 3.9, middle), it forms wider sheets of bilayer decorated by small patches of tri-layers and four-layers. On samples prepared over hot substrate (fig 3.9, right) or post-annealed, NaCl agglomerates on large three-dimensional blocks of several layers whose height easily exceeds ten atomic layers.

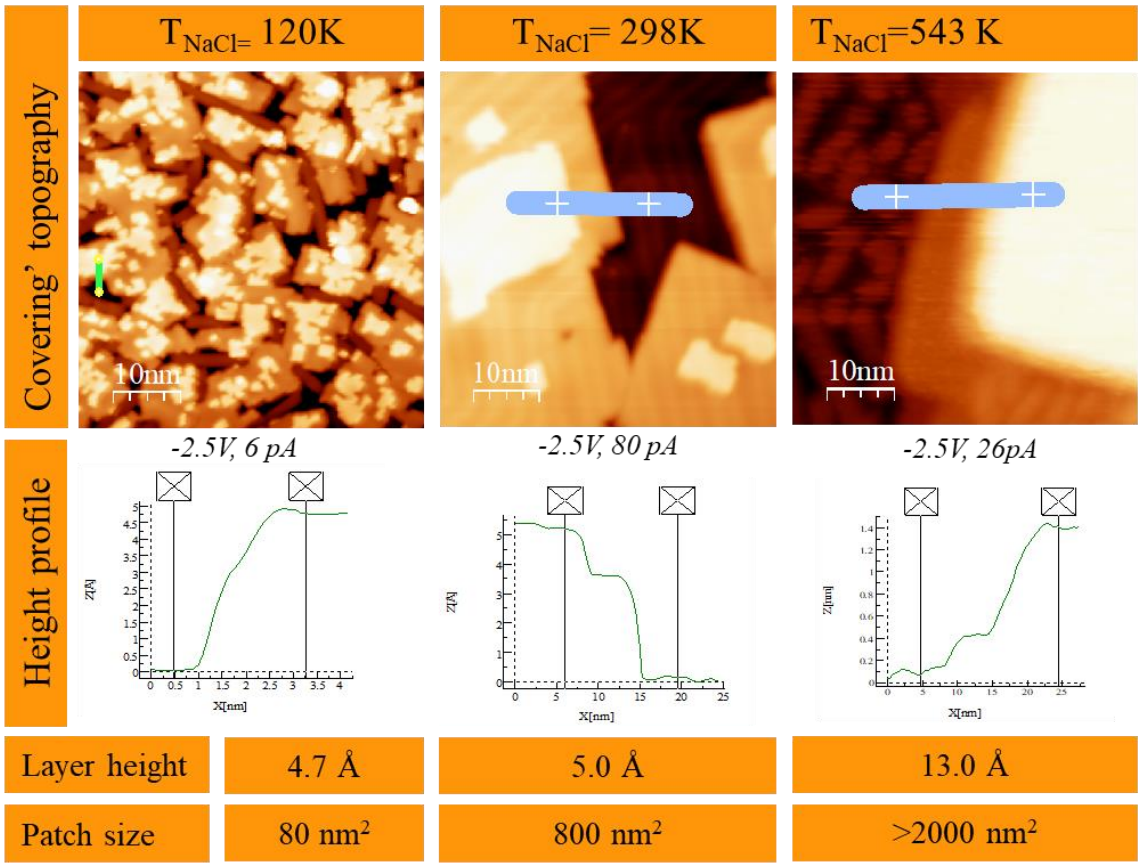

Figure 3.9. *Effect of temperature on the NaCl island formation after 1.8 ML of deposition.Left: The aggregation is quite irregular when salt is deposited onto a cold substrate (sample extracted 7 min from the STM at 4K before deposition). Middle: NaCl deposited with Au(111) kept at room temperature. The islands are much larger than in the previous case. Right: Sample heated up* T_{NaCl}*=270°C after RT deposition. The islands coalesce and grow in 3D, resulting in thicker layers.*

Although this effect cannot be observed *in-situ* on our STM due to its extremely cold working conditions, NaCl migrates over the surface by the thermal energy available at higher temperatures. Its tendency is to form big bulky blocks by means of coalescence (Fig 3.9, right), because the NaCl self-affinity overcomes its adsorption energy on Au(111), which implies that NaCl agglomeration is thermodynamically favourable.

3.1.3. Graphene nanoribbons and NaCl

3.1.3.1. NaCl deposition after ribbon formation

To grow the GNRs from the precursors by Ullmann reaction, the catalytic role of the Au surface is required[8,10,12,16,46]. For this reason, we always formed the GNRs on Au(111) prior to depositing NaCl. Two expected scenarios are possible when depositing NaCl over the GNRs: The intercalation of NaCl between ribbons and gold, or NaCl growth over both ribbons and gold.

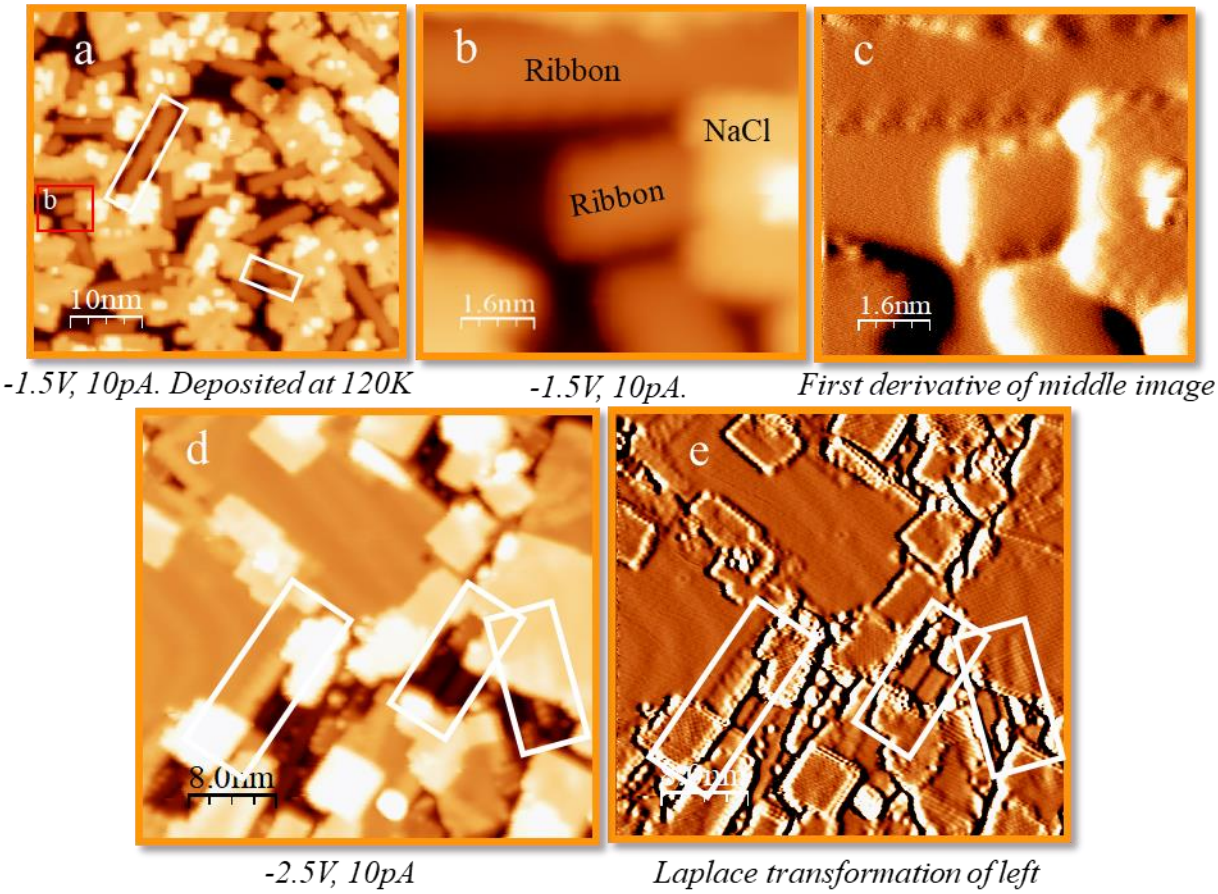

Figure 3.10. *Deposition of NaCl over GNR at low temperature* ***(a, b, c)*** *and at 298K* ***(d, e)****. STM images show that ribbons remain intact and are sandwiched between gold and salt. White rectangles mark several examples of ribbons under NaCl.* ***a)*** *Survey.* ***b)*** *Zoom of ribbons under salt.* ***c)*** *First derivative image (dz/dz) of (b), the contours of the ribbons' edges are visible, as well as hints of atomic resolution on NaCl.* ***d)*** *Survey with hidden ribbons.* ***e)*** *Laplace transformation displays herringbone reconstruction and ribbons (rectangles) underneath the NaCl.*

In our experiments, when NaCl is deposited over both cold and room temperature samples, we find that ribbons remain well bound (stuck) to the surface. Thus, NaCl sometimes covers the GNRs maintaining the structures previously seen. In Fig. 3.10, ribbons (observed as strips will dull brown contrast) are found sticking out and intercalating under the NaCl islands (Fig. 3.10 (a, d)). There is no chemical interaction observable between ribbons and salt. Ribbons remain intact under the ionic layers as shown by Fig 3.10 (c, e).

3.1.3.2. Annealing and lateral compression

This effect takes advantage of the mass displacement of NaCl over the gold with heat discussed in section 3.2.2. Annealing the samples with subsequent NaCl deposition after the synthesis of ribbons led to a large scale displacement of them from their original positions, as NaCl acts as a mechanical driving force associated to the thermal agitation of NaCl patches.

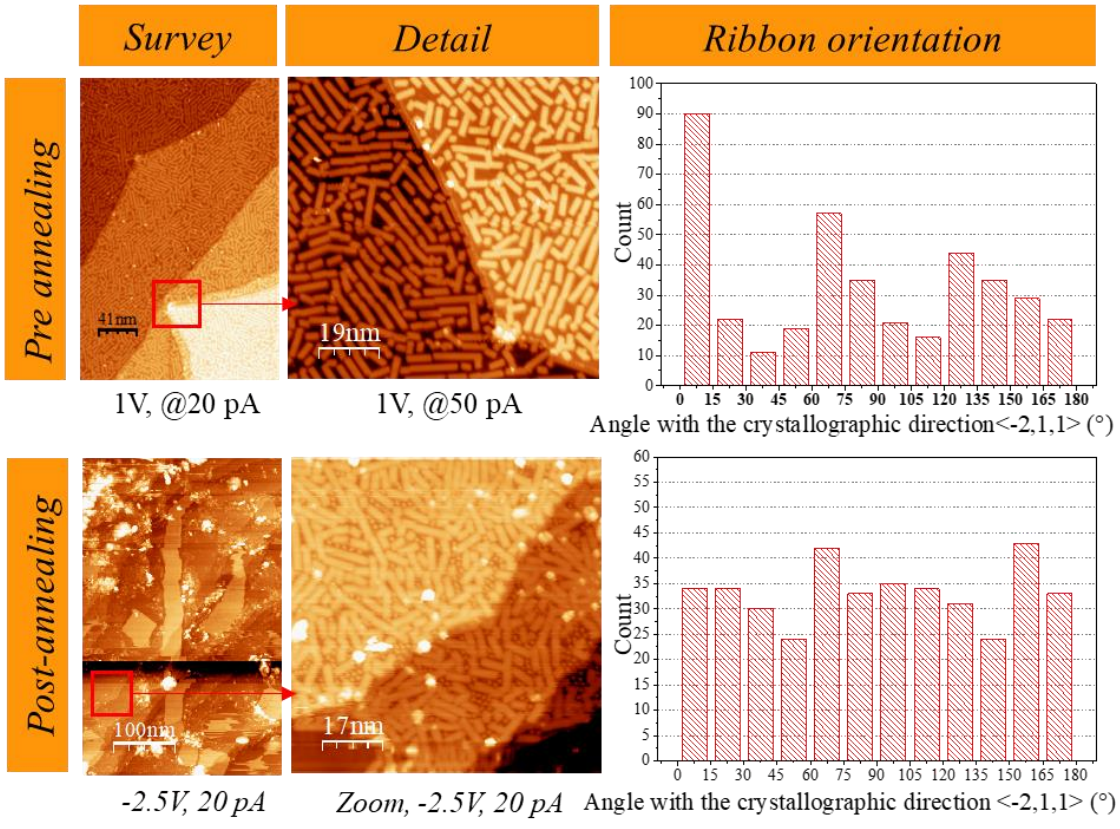

Figure 3.11. *Topside: Orientation of ribbons before salt+annealing. Downside: Ribbon orientation after salt deposition+annealing. Histograms were made measuring the orientation of 400 ribbons each, from 5 different areas taken from a 0.25 µm^2 survey.*

The NaCl patches or small grains (we could not determine the detail of the thermal agitation) drag and sweep the ribbons on its way to coalescence and form larger NaCl blocks as the one shown in Fig. 3.9. The ribbon displacement can be proven by comparing their preferred orientation before and after annealing.

Before annealing, the histogram in Fig 3.11 (top row) shows that they were preferably orientated at approximately 10º away from following the natural channels on Au (111) formed by the herring bone, which run along the <-2,1,1> crystallographic Au directions[29,55]. These channels form angles of 120° between them, and are perpendicular to the <0,1,-1> close packed directions of gold atoms on the surface. The angle formed by the ribbon axis and the lattice vectors of the graphene unit cell is 14º (See Fig 1.1). This means that the energetically most favourable stacking of the ribbons on Au is with the graphene lattice vectors parallel the Au <-2,1,1>. Such trend evidences a clear interaction between graphene lattice and Au electronic states[10].

In figure 3.12 (a), the evidences are proved experimentally. The measured ribbon fits perfectly on the orientation of Au(111) atoms. Notice that the distance between two graphene hexagons (twice its lattice constant, 4.92 Å) matches the distance between two Au atoms in the <-2,1,1> direction ($2 \cdot 2.89 \cdot \cos 30^{o} = 5.00$ Å) (Fig 3.12 (b)) [29,55].

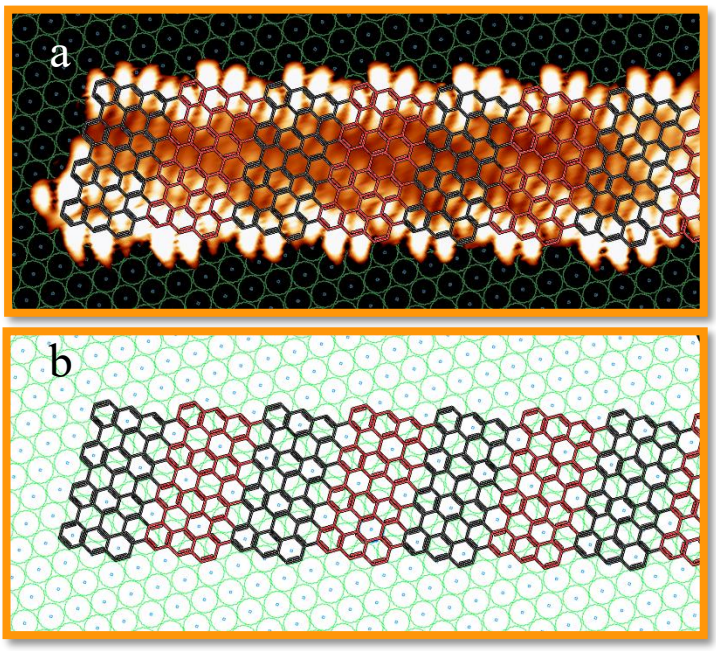

Fig 3.12. ***a)*** *Image of a ribbon taken with a functionalized tip and its relative orientation with the gold atomic closed packed directions, which were experimentally determined.*
b) *Model of the ribbon and Au (111). Gold' lattice orientation was obtained experimentally. The exact relative position of the atoms with the ribbon rings is an estimation.*

After annealing with NaCl, ribbons display a homogenous distribution of orientation (Fig. 3.11, bottom). Therefore, we can conclude that the ribbons have been swept across the surface by the mobile NaCl. This indicates that the NaCl transport due to thermal agitation at 270 ºC overcomes the absorption energy gain obtained by the preferred matching of the ribbons on bare Au(111). As shown in Fig. 3.11, bottom, the surface occupied by the agglomerated NaCl blocks is no longer available for the ribbons, which induces a denser packing of the ribbons or, as will be shown in the following, the piling of ribbons.

3.1.3.3. Ribbons on ribbons

Another effect of the thermal dragging of the ribbons by the NaCl: Some of them got mounted over others. Due to the high coverage of the Au (111) surface with ribbons, they had a small amount of free space per ribbon. Heating with NaCl forced them to move, carried by the salt, through the surface. A small fraction of them found an easier way to overcome the space limitations by stacking over other ribbons. These ribbons can be seen as brighter structures with a higher height (0.40nm at Vbias = -1V) than the one ascribed to the one graphene layer thickness (0.21 nm at Vbias = 1 V). Figure 3.13 shows how one of these higher strips lies on top of another ribbon, as proven by throwing the upper ribbon to the Au surface with the tip. The buried structure underneath the dropped ribbon is a regular (3,1)-cGNR on Au as the surrounding one.

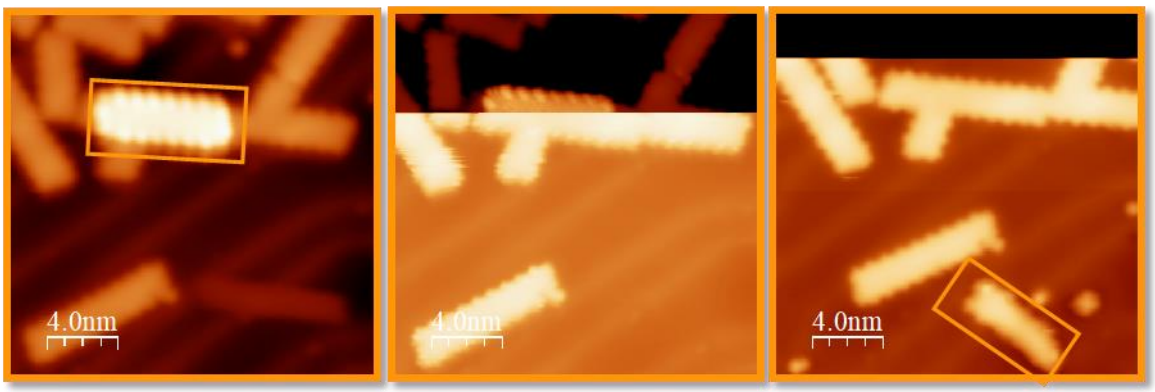

Figure 3.13. *Lateral compression of ribbons caused by NaCl agglomeration leads to vertical stacking of the GNRs that can be manipulated by the STM tip. a) The orange rectangle shows the initial configuration where a ribbon is found over another one. b) While scanning downwards, the upper ribbon is picked up by the tip and removed from its place (see contrast change as the tip becomes longer because of the ribbon). c) The ribbon is dropped later at the bottom of the image (orange box)*

3.2. ELECTRONIC PROPERTIES WITH AND WITHOUT DECOUPLING

In this section, the electronic properties of the (3,1)-cGNR synthesized will be studied. There are no previous reports about these ribbons, so they are interesting by themselves. Furthermore, the second part of this section compares the electronic resolution (spatial and energetic) of surface ribbons compared to over-gold ribbons, and it is going to leave evidence of the benefits of the developed decoupling method.

3.2.1. Edge states on cGNR/Au111

In the samples of ribbons over bare Au(111), three characteristic peaks have been identified:

1) Au(111) surface state (Fig 3.14, top row). It can be observed on the bare gold and it is commonly around -450 meV[27]. It is a 2D state confined to the Au surface caused by the truncation of the bulk.

2) A spectroscopic feature (a peak at around -200 meV) located in the central region of the ribbons. Since the GNRs are expected to be semiconducting and a similar peak was identified as the valence band in reported narrower chiral ribbons[8,10], we propose that this peak corresponds to the ribbons' valence band (fig 3.14, middle row). In these STS we can additionally find weaker Au states (around -400 meV).

3) Ribbons' edge states (fig 3.14, bottom row). The tight binding models predict that they are localized around the zig-zag graphene edges and in free standing GNRs should be symmetrically split around the Fermi level (inside the semiconducting gap), which is due to the Coulomb repulsion associated to the double occupancy of the edge state. On metals, however, the Coulomb repulsion by the substrate's conduction electrons, making the splitting much smaller and bringing the edge state peaks close to the Fermi level[25]. The periodic distribution of the peak near 20 meV coinciding with the ribbon' zigzag borders, and the sharpness of the peak, permits us to identify this feature as a graphene nanoribbon edge state

.

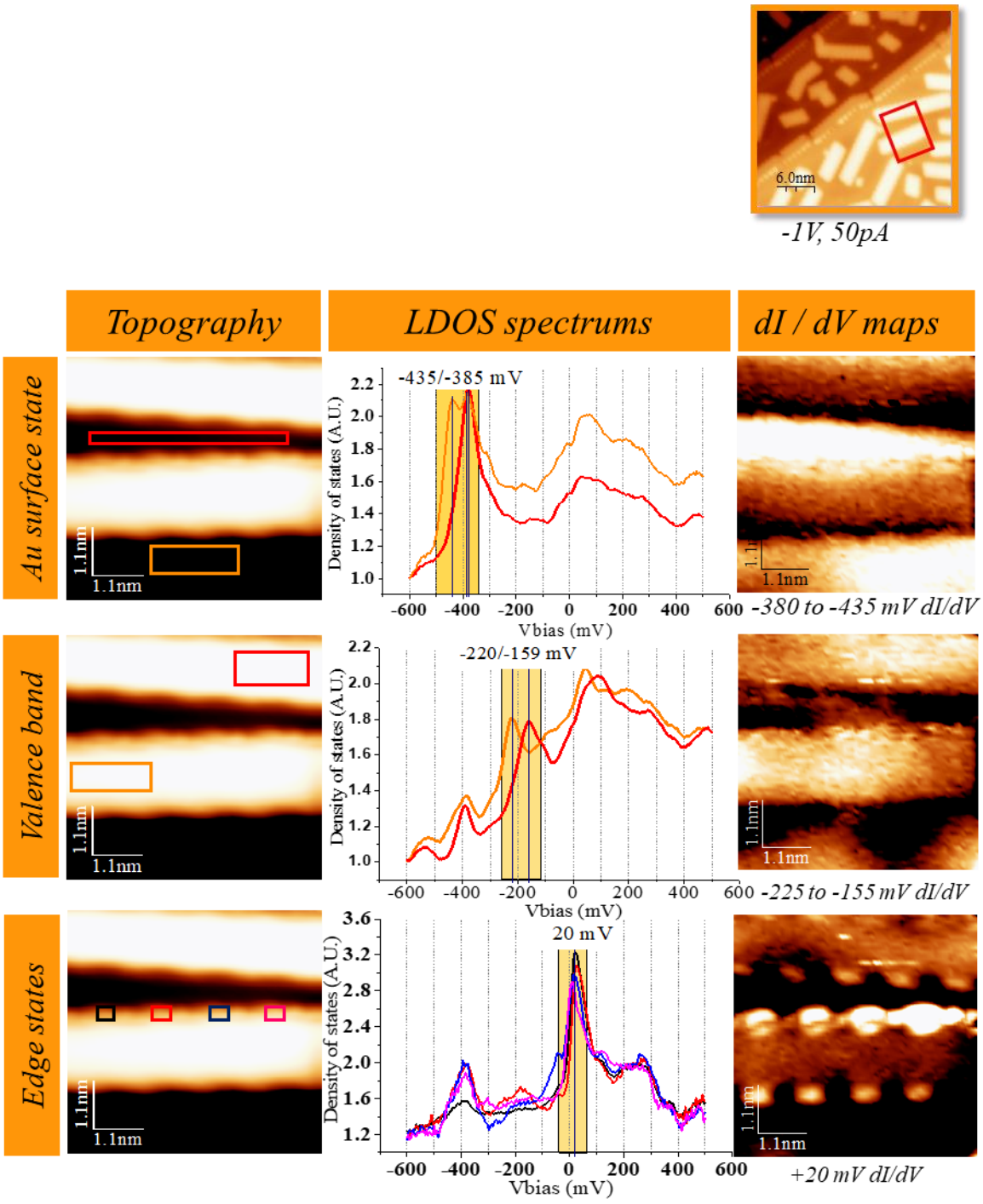

Figure 3.14. *Electronic structure of the GNRs on Au(111): Top) Surface state of the gold is located around -400 mV. Middle) Top of the GNRs' Valence band found around -200 mV. Bottom: Edge states are found near to the Fermi level. Setpoint: -1V, @200pA*

Fig 3.15 (1) shows a dedicated high resolution spectroscopy curve at the most intense LDOS spot of the assumed edge state, which shows its maximum intensity at 19 meV. The position of the peak fluctuates by a few meV in other positions of the same ribbon or at the edges of other ribbons (Fig 3.15). The full width at half maximum (FWHM) of the peak takes values in the range 60-150 meV, which for a discrete edge state implies significant broadening due to the hybridization with Au electrons.

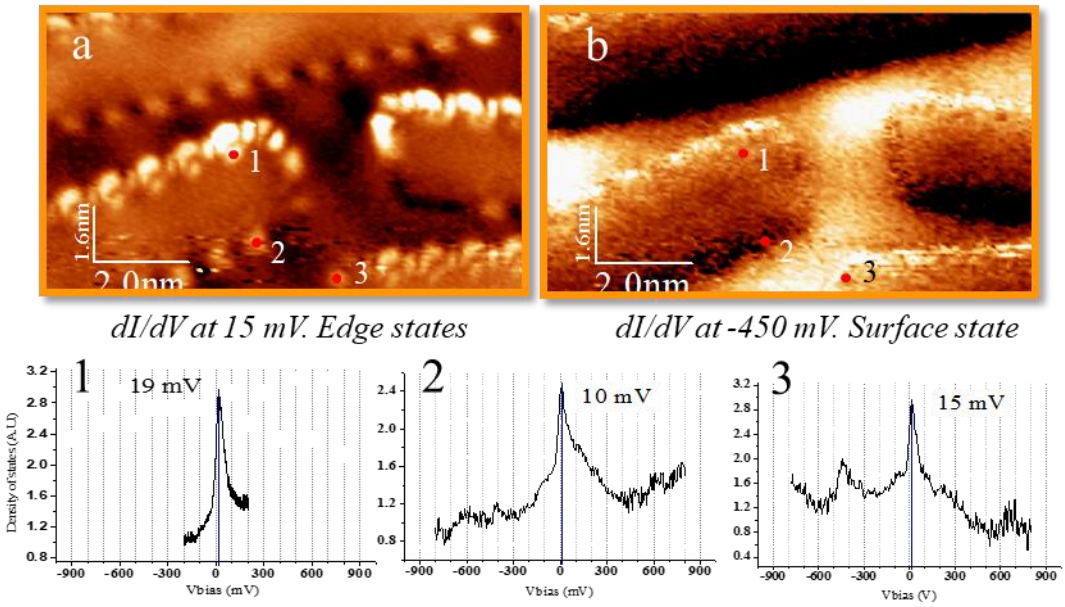

Figure 3.15. a) dI/dV map at 15 mV, shows edge state spatial distribution. b) dI/dV map of the gold' surface state. 1) His resolution spectroscopy of an *edge state LDOS*, found as a sharp, positive peak at *+19 mV. 2,3)* Other edge states are found at slightly different energies. 2) 10 mV, 3) 15mV. Setpoint: -1V, 200pA.

3.2.2. Comparison when decoupling nanoribbons.

The spectroscopic signatures found on GNRs on Au(111) are generally different from the decoupled ones. In the following we will consider the differences between ribbons directly in contact with the Au surface and ribbons over ribbons (stacked ribbons), as the one shown in Fig. 3.13. These occur after the thermal treatment of surrounding NaCl, as explained in section 3.1.3.3. The fingerprints of such ribbons readily identifiable in STM topographies is the increase in height and corrugation of the internal structure. As the stacked ribbons are decoupled from the Au(111), we find better spatial resolution in STM imaging and much better energy resolution in the STS spectroscopy.

3.2.2.1. Spatial resolution

Decoupling ribbons from the substrate increases the residence time of electrons in it, so they do not transfer immediately to the gold. This fact naturally decreases the hybridization with Au, causing the density of states of the ribbon to be more localized around the C atoms than in a free standing ribbon. This allows us to visualize the internal structure of the ribbon with a much greater resolution using gentle scanning conditions with metallic tips, so the ribbon' integrity is not compromised.

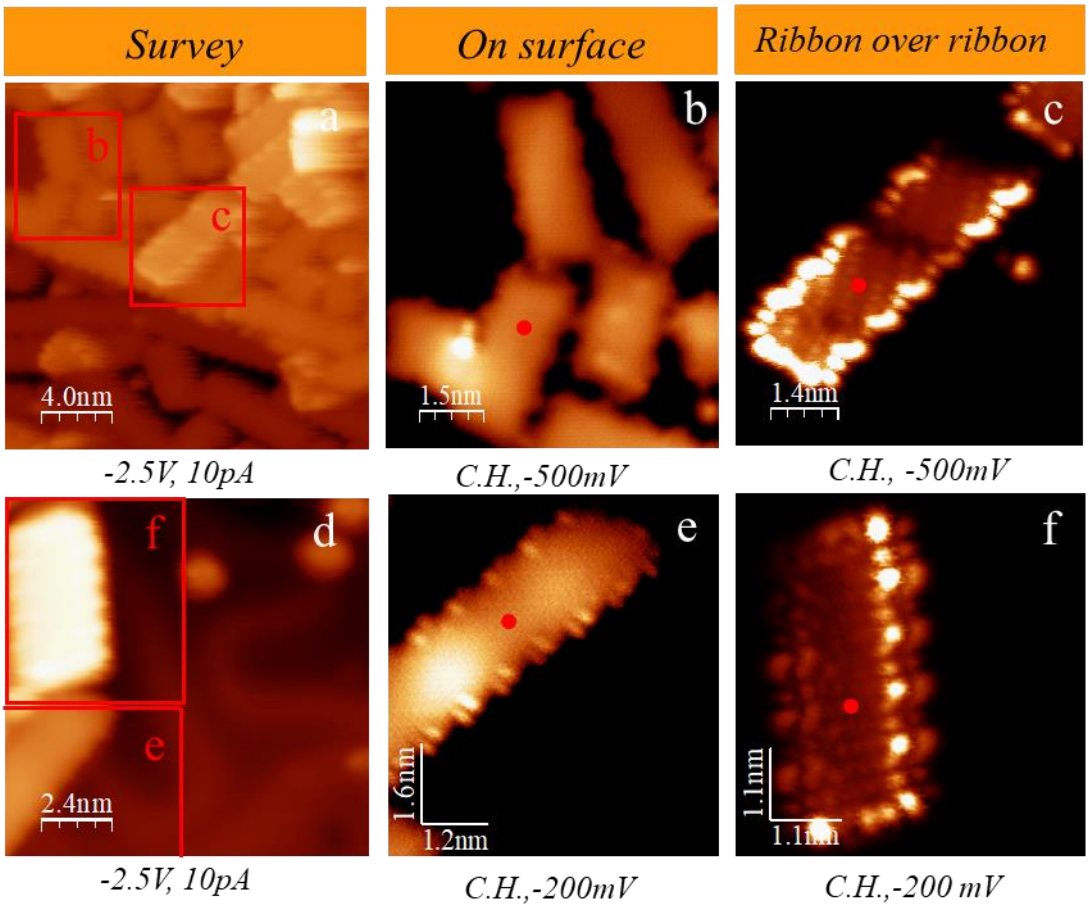

Figure 3.16. *Constant current topographs (a,d) and constant height tunneling current mages (b,c,e,f). Decoupling from gold orbitals reveal inner ribbon structures and highlight the edge state with mild scanning conditions. Both sets of images at bottom and top panels rows were taken systematically with identical tip conditions, Vbias and maximum tunneling currents at reference points (red dots) before opening the feedback (that is, identical tip-ribbon distance).*

Figure 3.16 displays a comparison of the STM resolution in constant height mode between GNR/Au and GNR/GNR/Au with a metallic Au tip. It is remarkable how, for the chosen experimental conditions, GNR/Au appears planar and homogeneous with maximum tunnelling current at its centre. On the other hand, stacked ribbons have an internal electronic structure, which is representative of their free-standing electronic structure[19]. This is the case of the inner pattern observed at -500 meV corresponding to the shape of the valence band wave function[8,10,19] (Fig 3.16 (c)).

In addition to presenting a clear graphene-like electronic structure spreading over the stacked ribbon, at -500 meV the edge displays the strongest intensity with a periodic pattern reminiscent of the edge states previously discussed. Probably, this is because the ribbons over gold have their valence band partially hybridized with Au conduction electrons, whereas the pure valence band states become visible when ribbon stacking decouples them from the substrate. Note that in Fig. 3.16 the edge intensity cannot be exclusively ascribed to edge states because the images are taken at energies too far from the Fermi level. The study of edge states of stacked ribbons will be addressed in subsection 3.2.2.2.

Furthermore, the stacking does not require to have the two ribbons perfectly aligned, so the ribbons can be partially exposed to the Au electronic states. Figure 3.17. illustrates examples of misaligned top and bottom ribbons. Note that decoupled ribbons are clearly identified by exhibiting structural appearance changes. In Fig. 3.17, panels (b) and (c) display the same behaviour in constant height (CH) conditions compared with the nearby GNR/Au of panel (a) acquired with the same tip. The increase in resolution only takes place in the regions with graphene underneath (red arrow in Fig 3.17 (d)), while in the bridging areas (yellow arrow Fig 3.17 (d)) the high spatial resolution of the electronic structure disappears.

Figure 3.17 (c) shows that the stacked ribbon fades away as the tip approaches the bridging region between the two ribbons straddled by the top ribbon. This gradual behaviour can be explained by the loss of rigidity and planarity of the top ribbon across the other two, resulting in a physical depression with valley shape contacting the gold at the deepest position. We also note that the occupied electronic states at the edges of decoupled ribbons are even visible at biases as high as -2.5 V (red arrow), whereas it fades out for the case of GNR/Au (yellow arrow), so the decoupling from the substrate can affect different areas of the same ribbon independently.

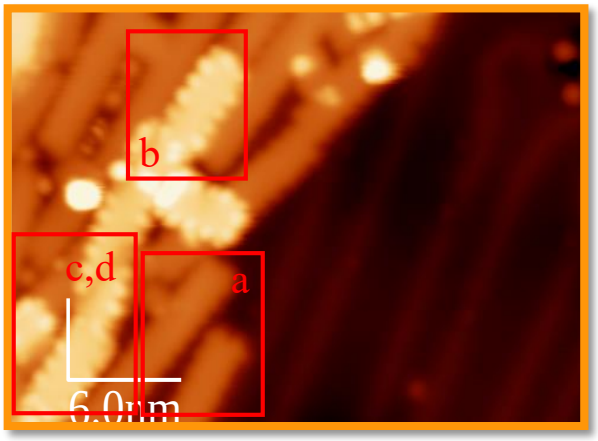

Figure 3.17. *-2.5V, 10 pA*
Long ribbon bridging over two ribbons

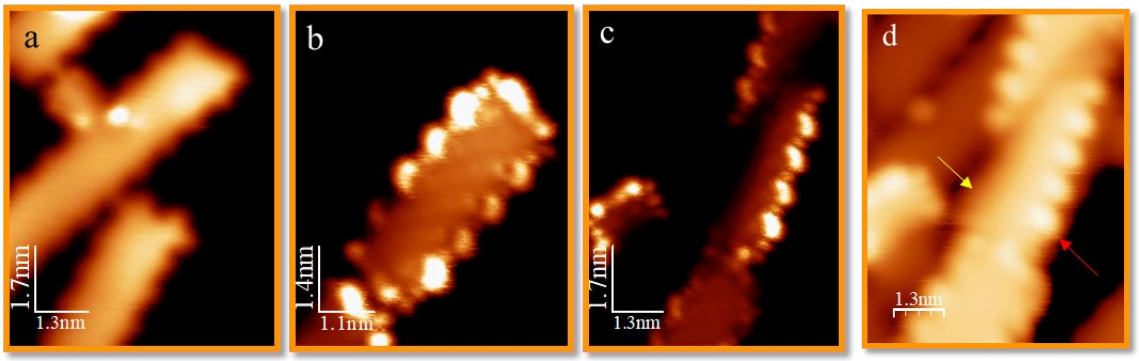

C.H. -500 mV *C.H. -500 mV* *C.H. -500 mV* *-2.5V, 10 pA*

Details of figure 3.17*. a) On surface ribbons b) Fully decoupled ribbon over ribbon. c) Ribbon mixing spatially coupled and uncoupled states. In (c), the left side of the image shows a short ribbon with half side over the Au surface and the other side on top of another ribbon. On the right side, the long ribbon hangs between two ribbons. d) Lobes disappear on the edges which are in contact with Au (111). Yellow arrow marks the on-gold edge and red arrow indicates the decoupled edge.*

3.2.2.2. Energy resolution of edge state and valence band onset.

As indicated in section 2.2, the STM feedback makes use of the total density of states from the Fermi level to a chosen Vbias for fixing the tip height. The lower electronic density of decoupled ribbons approaches the tip closer to the nanostructure so the states are visualised as more intense and sharper than when in direct contact to the substrate. Therefore, the correspondingly lower DOS background increases the relative weight of the ribbons' states and its spatial resolution, as discussed in the previous subsection.

Nonetheless, aside from the improved spatial resolution, decoupling the ribbons from the substrate also decreases the energy uncertainty of the electronic states. This is equivalent to increasing the residence time of a tunnelling electron in the ribbon before decaying into the Au surface. This relates to the fact that decoupling breaks the electronic hybridization of the ribbon orbitals with the gold orbitals, which entails an electronic change that affects the ribbon wave function, as well as the electronic configuration of the ribbon causing different LDOS for stacked ribbons in comparison to GNR/Au. In particular, due to the decreased spread in energy, electronic decoupling must provoke a sharpening in energy of the dI/dV spectroscopic features.

Using a very sharp metal tip capable of resolving the ribbons' electronic structure (see Fig. 3.18 (b), the edge state of GNR/Au is barely visible and poorly defined in energy, as shown in Fig 3.18 (2). At lower energies where the valence band onset is expected, the dI/dV spectrum is featureless. In contrast, when the same tip is used to acquire the energy resolved LDOS of the stacked (and decoupled) ribbon, much better defined features are observed (see Fig 3.18 (3)). The edge state lineshape becomes very sharp with FWHM of about 30 meV (compare to the regular edge state shown in section 3.2.1). The valence band onset at -160 meV is also visible, with a sharp step-like feature at -180 meV.

As expected, the spatial resolution of the edge state wave function is much better for the decoupled case. The electronic corrugation of the edge state wave function is more pronounced in the case of the stacked ribbon, revealing the its internal structure in detail (Fig 3.18 (b)).

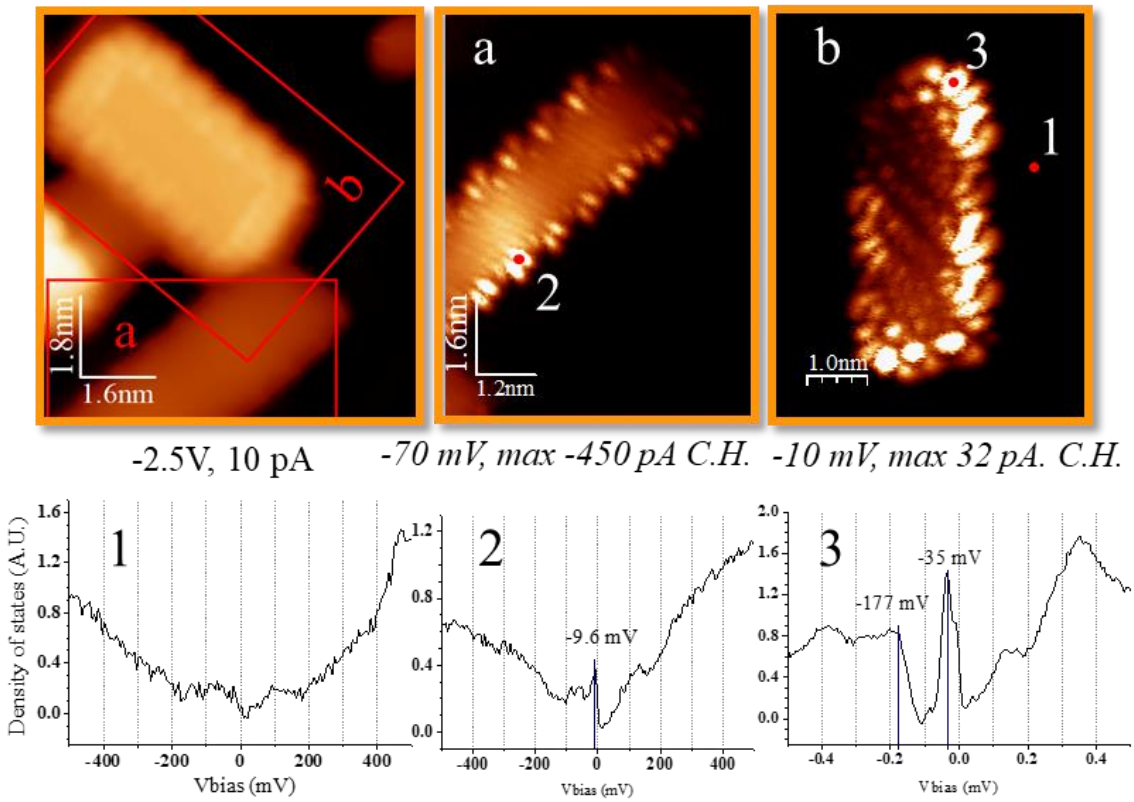

*º**Figure 3.18.** Comparing sensibilities and resolutions: **a)** On-surface ribbon. **b)** Stacked ribbon. **1)** Gold spectrum **2)** LDOS of on-surface ribbon' edge state.. **3)** Stacked ribbon' LDOS spectra. Decoupling from the substrate causes valence band onset (-177 mV) & edge state peak (-35mV) to seem more intense and sharp. All three images & spectra were taken with the same tip and offset. Setpoint: -1V, 50pA*

4. CONCLUSIONS

A new type of chiral nanoribbon, the (3,1)-cGNR, has been successfully synthesised from dBQA precursors. This molecular precursors, the subsequent polimerization steps and the nanoribbons were structurally confirmed by topographic STM images. Specifically, the period and internal structures have been confirmed using topography imaging with normal metallic tips and functionalized ones, which verified to match the theoretical calculations. Furthermore, its electronic properties have been successfully studied, and the higher part of its valence ban, as well as the presence of edge states in the vicinity of the Fermi level have been confirmed.

In addition, the NaCl growth and response to temperature after deposition onto Au(111) showed different density agglomeration into islands. This effect, in presence of cGNR caused a generalized displacement of the molecular structures, affecting its orientation with respect to the substrate and causing some of them to stack on top of other cGNRs. This resulted in an effective ribbon decoupling from the metallic substrate, which increased the energy and spatial resolution when studying the ribbons, both on the STM images and the STS spectra. This allowed us to investigate its internal electronic structure without the need for functionalising the tip. Indeed, the performance of a regular metal tip on stacked ribbons parallels the one of functionalized tips on a metal surface, making the burdensome process of tip functionalization unnecessary. In the STS spectra, the decoupling caused a sharpening of the bands that allows its proper identification.

As outlook, we propose to use this decoupling method as a simple technique to study the electronic structure of the edge states in cGNR, or as a tool to spontaneously detach the ribbons from the substrate for a possible transferring method to Si-based substrates GNRs on a larger scale, bridging the gap between on-surface synthesis and electronic applications.

5. REFERENCES

1. Garcia-Sanchez, D. *et al.* Imaging mechanical vibrations in suspended graphene sheets. *Nano Lett.* **8,** 1399–1403 (2008).
2. Eichler, A. *et al.* Nonlinear damping in mechanical resonators made from carbon nanotubes and graphene. *Nat. Nanotechnol.* **6,** 339–342 (2011).
3. Wang, J., Wang, X., Xu, C., Zhang, M. & Shang, X. Preparation of graphene/poly(vinyl alcohol) nanocomposites with enhanced mechanical properties and water resistance. *Polym. Int.* **60,** 816–822 (2011).
4. Hwang, E. H., Adam, S. & Sarma, S. Das. Carrier transport in two-dimensional graphene layers. *Phys. Rev. Lett.* **98,** 2–5 (2007).
5. Pumera, M. Graphene-based nanomaterials for energy storage. *Energy Environ. Sci.* **4,** 668–674 (2011).
6. Wang, Y., Tong, S. W., Xu, X. F., Özyilmaz, B. & Loh, K. P. Interface engineering of layer-by-layer stacked graphene anodes for high-performance organic solar cells. *Adv. Mater.* **23,** 1514–1518 (2011).
7. Miao, X. *et al.* High Efficiency Graphene Solar Cells by Chemical Doping. 6–11 (2012).
8. Merino-Díez, N. *et al.* Width-Dependent Band Gap in Armchair Graphene Nanoribbons Reveals Fermi Level Pinning on Au(111). *ACS Nano* **11,** 11661–11668 (2017).
9. Verónica Barone *et al.* Electronic Structure and Stability of Semiconducting Graphene Nanoribbons. *Nano Lett.* **6,** 2748–2754 (2006).
10. Merino-Díez, N. *et al.* Unraveling the Electronic Structure of Narrow Atomically Precise Chiral Graphene Nanoribbons. *J. Phys. Chem. Lett.* **9,** 25–30 (2018).
11. Huang, X. *et al.* Graphene-based materials: Synthesis, characterization, properties, and applications. *Small* **7,** 1876–1902 (2011).
12. Moreno, C. *et al.* Bottom-up synthesis of multifunctional nanoporous graphene. *Science (80-.).* **360,** 199–203 (2018).
13. Cai, J. *et al.* Atomically precise bottom-up fabrication of graphene nanoribbons. *Nature* **466,** 470–473 (2010).
14. Wang, S. *et al.* Giant edge state splitting at atomically precise graphene zigzag edges. *Nat. Commun.* **7,** 3–8 (2016).

15. Grill, L. *et al.* Nano-architectures by covalent assembly of molecular building blocks. *Nat. Nanotechnol.* **2,** 687–691 (2007).
16. Massimi, L. *et al.* Surface-assisted reactions toward formation of graphene nanoribbons on Au(110) surface. *J. Phys. Chem. C* **119,** 2427–2437 (2015).
17. Repp, J., Meyer, G., Stojković, S. M., Gourdon, A. & Joachim, C. Molecules on insulating films: Scanning-tunneling microscopy imaging of individual molecular orbitals. *Phys. Rev. Lett.* **94,** 1–4 (2005).
18. Gutzler, R. *et al.* Surface mediated synthesis of 2D covalent organic frameworks: 1,3,5-tris(4-bromophenyl)benzene on graphite(001), Cu(111), and Ag(110). *Chem. Commun.* **0,** 4456–4458 (2009).
19. Jacobse, P. H., Mangnus, M. J. J., Zevenhuizen, S. J. M. & Swart, I. Mapping the Conductance of Electronically Decoupled Graphene Nanoribbons. *ACS Nano* **12,** 7048–7056 (2018).
20. Ruffieux, P. *et al.* On-surface synthesis of graphene nanoribbons with zigzag edge topology. *Nature* **531,** 489–492 (2016).
21. Kawai, S. *et al.* Supplementary Information for Superlubricity of graphene nanoribbons on gold surfaces. *Science* **351,** 957–961 (2016).
22. K. S. Novoselov, 1 A. K. Geim, 1* S. V. Morozov, 2 D. Jiang, 1 Y. Zhang, 1 S. V. Dubonos, 2 I. V. Grigorieva, 1 A. A. Firsov. Electric Field Effect in Atomically Thin Carbon Films. *Science* **306,** 666–669 (2004).
23. Koch, M., Ample, F., Joachim, C. & Grill, L. Voltage-dependent conductance of a single graphene nanoribbon. *Nat. Nanotechnol.* **7,** 713–717 (2012).
24. Hebenstreit, W. *et al.* Atomic resolution by STM on ultra-thin films of alkali halides: Experiment and local density calculations. *Surf. Sci.* **424,** (1999).
25. Tao, C. *et al.* Spatially resolving edge states of chiral graphene nanoribbons. *Nat. Phys.* **7,** 616–620 (2011).
26. Ernst, K. H. Molecular chirality in surface science. *Surf. Sci.* **613,** 1–5 (2013).
27. Chen, W., Madhavan, V., Jamneala, T. & Crommie, M. F. Scanning tunneling microscopy observation of an electronic superlattice at the surface of clean gold. *Phys. Rev. Lett.* **80,** 1469–1472 (1998).
28. Yazyev, O. V., Capaz, R. B. & Louie, S. G. Theory of magnetic edge states in chiral graphene nanoribbons. *Phys. Rev. B - Condens. Matter Mater. Phys.* **84,** 1–5 (2011).
29. Son, Y. W., Cohen, M. L. & Louie, S. G. Half-metallic graphene nanoribbons.

Nature **444,** 347–349 (2006).

30. Pan, M. *et al.* Topographic and Spectroscopic Characterization of Electronic Edge States in CVD Grown Graphene Nanoribbons. *Nano Lett.* **12,** 1928–1933 (2012).
31. Repp, J., Meyer, G., Paavilainen, S., Olsson, F. E. & Persson, M. Imaging Bond Formation Between a. *Science (80-.).* **1196,** 1196–1199 (2010).
32. Bombis, C. *et al.* Single molecular wires connecting metallic and insulating surface areas. *Angew. Chemie - Int. Ed.* **48,** 9966–9970 (2009).
33. Li, Z. *et al.* Chemically modified STM tips for atomic-resolution imaging of ultrathin NaCl films. *Nano Res.* **8,** 2223–2230 (2015).
34. Gross, L. Recent advances in submolecular resolution with scanning probe microscopy. *Nat. Chem.* **3,** 273–278 (2011).
35. Repp, J. & Meyer, G. Scanning tunneling microscopy of adsorbates on insulating films. from the imaging of individual molecular orbitals to the manipulation of the charge state. *Appl. Phys. A Mater. Sci. Process.* **85,** 399–406 (2006).
36. Binnig, G., Rohrer, H., Gerber, C. & Weibel, E. Surface studies by scanning tunneling microscopy. *Phys. Rev. Lett.* **49,** 57–61 (1982).
37. Kim, P., Odom, T. W., Huang, J. & Lieber, C. M. STM study of single-walled carbon nanotubes. *Carbon N. Y.* **38,** 1741–1744 (2000).
38. Wiesendanger, R. Spin mapping at the nanoscale and atomic scale. *Rev. Mod. Phys.* **81,** 1495–1550 (2009).
39. Kubetzka, A. *et al.* Revealing antiferromagnetic order of the Fe monolayer on W(001): Spin-polarized scanning tunneling microscopy and first-principles calculations. *Phys. Rev. Lett.* **94,** 2–5 (2005).
40. Guo, Q., Yin, F. & Palmer, R. E. Beyond the herringbone reconstruction: Magic gold fingers. *Small* **1,** 76–79 (2005).
41. Langlais, V. J. *et al.* Spatially resolved tunneling along a molecular wire. *Phys. Rev. Lett.* **83,** 2809–2812 (1999).
42. Ding, Y., Xie, L., Zhang, C. & Xu, W. Real-space evidence of the formation of the GCGC tetrad and its competition with the G-quartet on the Au(111) surface. *Chem. Commun.* **53,** 9846–9849 (2017).
43. Van de Leemput, L. E. C., van Kempen, H., Scanning tunnelling microscopy *Rep. Progr. Phys.* **55,** 1165 (1992).
44. Moro-Lagares, M. Engineering Spin Structures at the Atomic Scale. *PhD Thesis,*

Universidad de Zaragoza (2015).

45. Camillone, N. *et al.* New monolayer phases of n-alkane thiols self-assembled on Au(111): Preparation, surface characterization, and imaging. *J. Chem. Phys.* **101,** 11031–11036 (1994).
46. Ullmann, F. Ueber Synthesen in der Carbazolgruppe. *Berichte der Dtsch. Chem. Gesellschaft* **31,** 1697–1698 (1898).
47. Orpen, A. G. *et al.* Tables of Bond Lengths determined by X-Ray and Neutron Diffraction. *J. Chem. Soc. Dalt. Trans.* S1–S83 (1987).
48. Peyrot, D. & Silly, F. Enhancing intramolecular features and identifying defects in organic and hybrid nanoarchitectures on a metal surface at room temperature using a NaCl-functionalized scanning tunneling microscopy tip. *RSC Adv.* **7,** 51055–51061 (2017).
49. Bombis, C. *et al.* Hydrogen-bonded molecular networks of melamine and cyanuric acid on thin films of naCl on au(111). *Small* **5,** 2177–2182 (2009).
50. Glöckler, K., Sokolowski, M., Soukopp, A. & Umbach, E. Initial growth of insulating overlayers of NaCl on Ge(100) observed by scanning tunneling microscopy with atomic resolution. *Phys. Rev. B* **54,** 7705 (1996).
51. Martinez-Castro, J. *et al.* Electric polarization switching in an atomically thin binary rock salt structure. *Nat. Nanotechnol.* **13,** 19–23 (2018).
52. Hebenstreit, W., Schmid, M., Redinger, J., Podloucky, R. & Varga, P. Bulk terminated NaCl(111) on aluminum: a polar surface of an ionic crystal? *Phys. Rev. Lett.* **85,** 5376–5379 (2000).
53. Pivetta, M., Patthey, F., Stengel, M., Baldereschi, A. & Schneider, W. D. Local work function Moiré pattern on ultrathin ionic films: NaCl on Ag(100). *Phys. Rev. B - Condens. Matter Mater. Phys.* **72,** 1–6 (2005).
54. Peyrot, D. & Silly, F. Temperature-Dependent Structure of Two-Dimensional Hybrid NaCl-PTCDI Nanoarchitectures on Au(111). *J. Phys. Chem. C* **121,** 20986–20993 (2017).
55. Schouteden, K., Lievens, P. & Van Haesendonck, C. Fourier-transform scanning tunneling microscopy investigation of the energy versus wave vector dispersion of electrons at the Au(111) surface. *Phys. Rev. B - Condens. Matter Mater. Phys.* **79,** 1–7 (2009).
56. Kumazaki, H. & Hirashima, D. S. Local magnetic moment formation on edges of graphene. *J. Phys. Soc. Japan* **77,** 1–5 (2008).

6. ANNEXES:

6.1. Acronym index.

A.U. .....Arbitrary Units

cGNR……chiral Graphene NanoRibbons

dBQA……....2”,3’-dibromine-9,9’:10’,9”:10”,9”’-quateranthracene

DOS……..Density of States

GNR……..Graphene NanoRibbons

FWHM……..... Full Width at Half Maximum

LDOS……Local Density of States

ML/min…….Monolayers per minute

STM……..Scanning Tunnelling Microscopy

STS……...Scanning Tunnelling Spectroscopy

UHV…….Ultra High Vacuum

CH…… Constant height